ACS NANO

www.acsnano.org

ARTICLE

Machine Learning-Powered Ultrahigh Controllable and Wearable Magnetoelectric Piezotronic Touching Device

Xingjuan Song, Bao Yi, Qijun Chen, Yifei Zhou, Hyeon Cho, Yongtaek Hong, Seungjun Chung, Long You, Shaofan Li, and Jeongmin Hong*

Cite This: *ACS Nano* 2024, 18, 16648−16657

Read Online

ACCESS | Metrics & More | Article Recommendations | Supporting Information

ABSTRACT: **Recent advancements in nanomaterials have enabled the application of nanotechnology to the development of cutting-edge sensing and actuating devices. For instance, nanostructures' collective and predictable responses to various stimuli can be monitored to determine the physical environment of the nanomaterial, such as temperature or applied pressure. To achieve optimal sensing and actuation capabilities, the nanostructures should be controllable. However, current applications are limited by inherent challenges in controlling nanostructures that counteract many sensing mechanisms that are reliant on their area or spacing. This work presents a technique utilizing the piezo-magnetoelectric properties of nanoparticles to enable strain sensing and actuation in a flexible and wearable patch. The alignment of nanoparticles has been achieved using demagnetization fields with computational simulations confirming device characteristics under various types of deformation followed by experimental demonstrations. The device exhibits favorable piezoelectric performance, hydrophobicity, and body motion-sensing capabilities, as well as machine learning-powered touch-sensing/actuating features.**

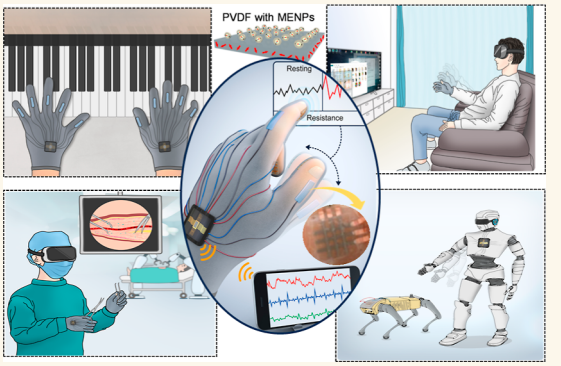

KEYWORDS: *multiferroics, magnetoelectric nanoparticles, P(VDF-TrFE), $BaTiO_3$@$CoFe_2O_4$, flexible*

INTRODUCTION

Multiferroic materials, which exhibit the coexistence of (anti)ferromagnetism, ferroelectricity, and ferroelasticity, have garnered significant attention due to their diverse ferroic orderings and resultant magnetoelectric effect. The past few decades have seen multiferroic materials extensively studied in the pursuit of high-performance electronic devices.[1−5] Recently discovered nanoparticle types include organic nanoparticles (NPs) such as liposomes and polymeric NPs, along with inorganic NPs like quantum dots, graphene, magnetic NPs, and metal NPs,[6−15] among others. These nanoparticles may be employed for various nanocontrolled release systems that respond to thermal, optical (ultraviolet), electrochemical, or ultrasound stimuli.[16−28]

Core−shell composite multiferroic (MF) NPs are capable of low-field on-demand actuation owing to their magnetoelectric (ME) coupling effect—a feature distinct from traditional magnetic NPs—thereby offering advantages such as low loss and high energy efficiency.[29−32] Consequently, wearable or implantable systems can benefit from nanocontrolled sensing/actuating based on these magnetoelectric nanoparticle (MENP) technologies.[33,34] Strain-mediated indirect ME coupling occurs when magnetic/electric order parameters arise in separate but intimately connected phases within a given material. Furthermore, multifunctional NP-based solutions show promise across several applications; however, controlling NPs make issues arising from easy agglomeration limit their practical use cases. Wearable sensors/actuators hold great potential toward targeted drug delivery/monitoring; nevertheless, nanomaterials pose challenges when it comes to fabricating nanostructures onto soft substrates while maintaining stability/sensitivity conditions required for highly accurate devices.[33−39]

To address this challenge, we present an effective approach utilizing flexible MENP-deposited patches, which enable us to

Received: January 23, 2024
Revised: May 15, 2024
Accepted: May 24, 2024
Published: June 18, 2024

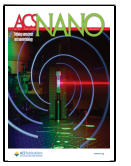

https://doi.org/10.1021/acsnano.4c01102
ACS Nano 2024, 18, 16648−16657

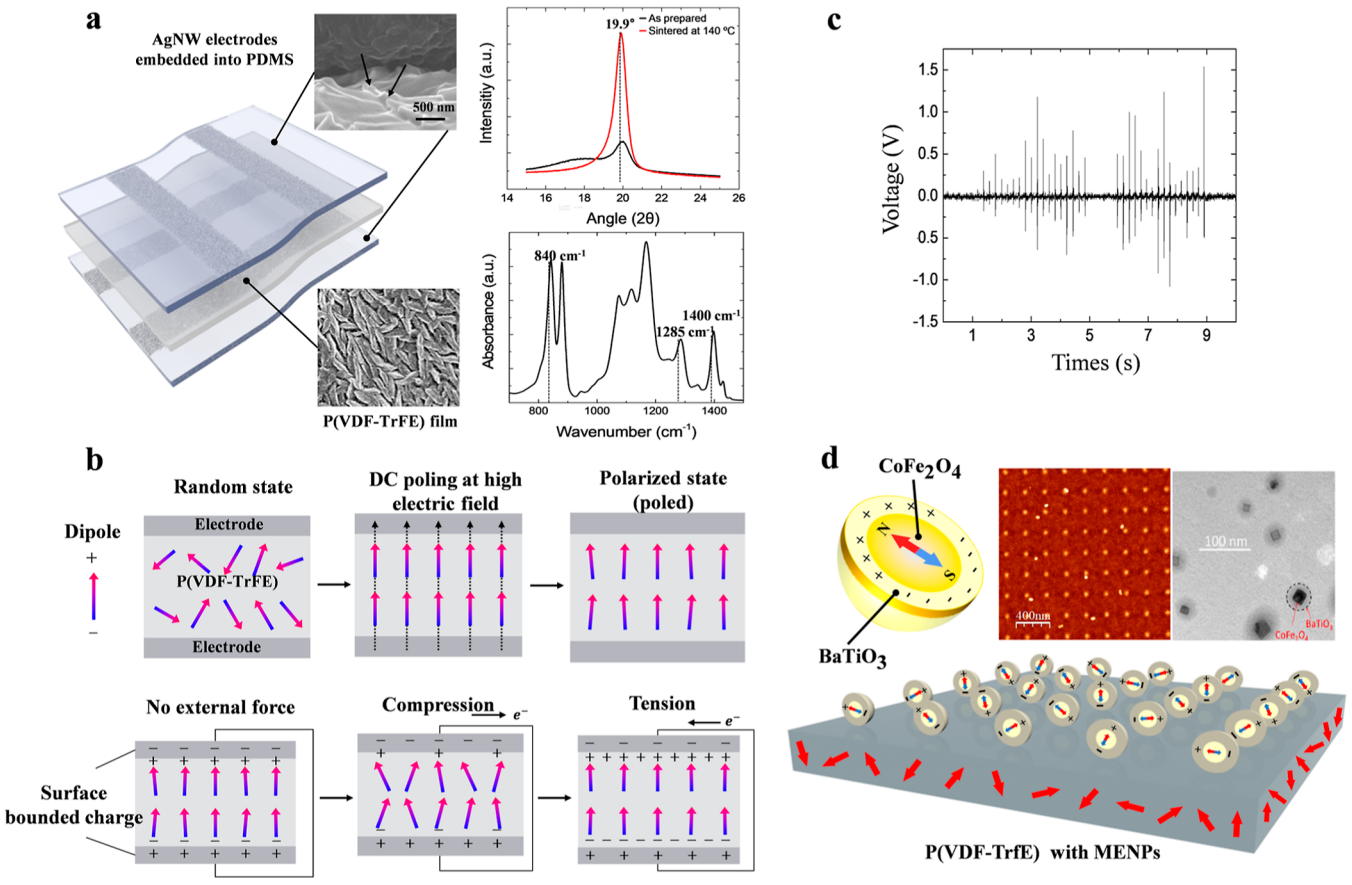

Figure 1. Piezoelectric performance of soft piezoelectric devices. (a) Conceptual illustration of a soft piezoelectric device composed of AgNW electrodes and a P(VDF-TrFE) piezoelectric film. Scanning electron microscopy (SEM) images show the embedded AgNW networks in a PDMS soft substrate and well-crystallized P(VDF-TrFE) film. The XRD and FTIR spectra of P(VDF-TrFE). The XRD spectra show the peaks under different sintering time conditions and confirm the β-phase of P(VDF-TrFE), for that the peak at 2θ = 20.26° is related to the diffraction of β-phase at (110) and (200). FTIR spectra show that vibrational bands at 840, 1279, and 1400 cm^{-1} correspond to the β-phase of P(VDF-TrFE). (b) Schematic illustration of the high-voltage poling process of the piezoelectric device and its piezoelectric operation under mechanical deformation. (c) Piezoelectric performance of the poled piezoelectric device. (d) Piezoelectric field-assisted magnetization switching of the MENP device. Schematics of the ME particles. Atomic force microscopy (AFM) and transmission electron microscopy (TEM) show the patch after the deposition of ME particles.

create an ultrasensitive/highly controllable wearable magneto-electric-piezoelectric (ME-PZT) switch. Our optimized deposition process ensures core−shell NP alignment via demagnetization fields thus avoiding any agglomeration issues.[40] To confirm device physical characteristics upon deformation under varying conditions, computational simulations were conducted alongside experimental demonstrations showing favorable piezoelectric performance coupled with super-hydrophobicity/body motion-sensing capabilities.[40] The resulting machine learning-powered sensing and actuating system is demonstrated using the patch for metaverse applications.[41]

RESULTS

First, we optimize the design and fabrication of wearable substrates composed of stretchable interconnects embedded on an elastomer substrate and a piezoelectric film. To provide high conductive and mechanical tolerance under various deformations for stretchable sensors, silver nanowire (AgNW) network-based nanocomposites are used as intrinsically stretchable interconnects and polydimethylsiloxane (PDMS) is used as the supporting material,[42] as shown in Figure 1a. In the top right image, AgNW networks are well dispersed in PDMS. For the manipulation of the magnetic properties of the multiferroic NPs via the generated E-field, poly(vinylidene fluoride-trifluoro ethylene) [P(VDF-TrFE)] is employed due to its ability to convert mechanical stimuli into electricity.[43,44] Different electric fields generated through applying various stresses or strains to PVDF have been simulated, as can be seen in Supporting Information Figure S1. To achieve wearable properties and controllable functions, the flexibility and inverse electric effect of P(VDF-TrFE) also have been utilized; so, a high-quality flexible β-phase P(VDF-TrFE) film needs to be made to form a flexible substrate (see details in Supporting Information Figure S2). The high-density β-phase was successfully achieved under different sintering temperatures and times, and the optimized sintering condition is 140 °C for 1 h verified by the X-ray diffraction (XRD) in Supporting Information Figure S3, which has also been verified by the Fourier transform infrared (FTIR) measurement, as shown in Figure 1a. XRD shows that the peak lies at 2θ = 19.9°, FTIR shows the absorbance of the vibrational bands at 840, 1285, and 1400 cm^{-1}, and all peaks correspond to the β-phase, which could in turn result in a high piezoelectric coefficient and uniformly generate an electric field in P(VDF-TrFE).[45]

https://doi.org/10.1021/acsnano.4c01102
ACS Nano 2024, 18, 16648−16657

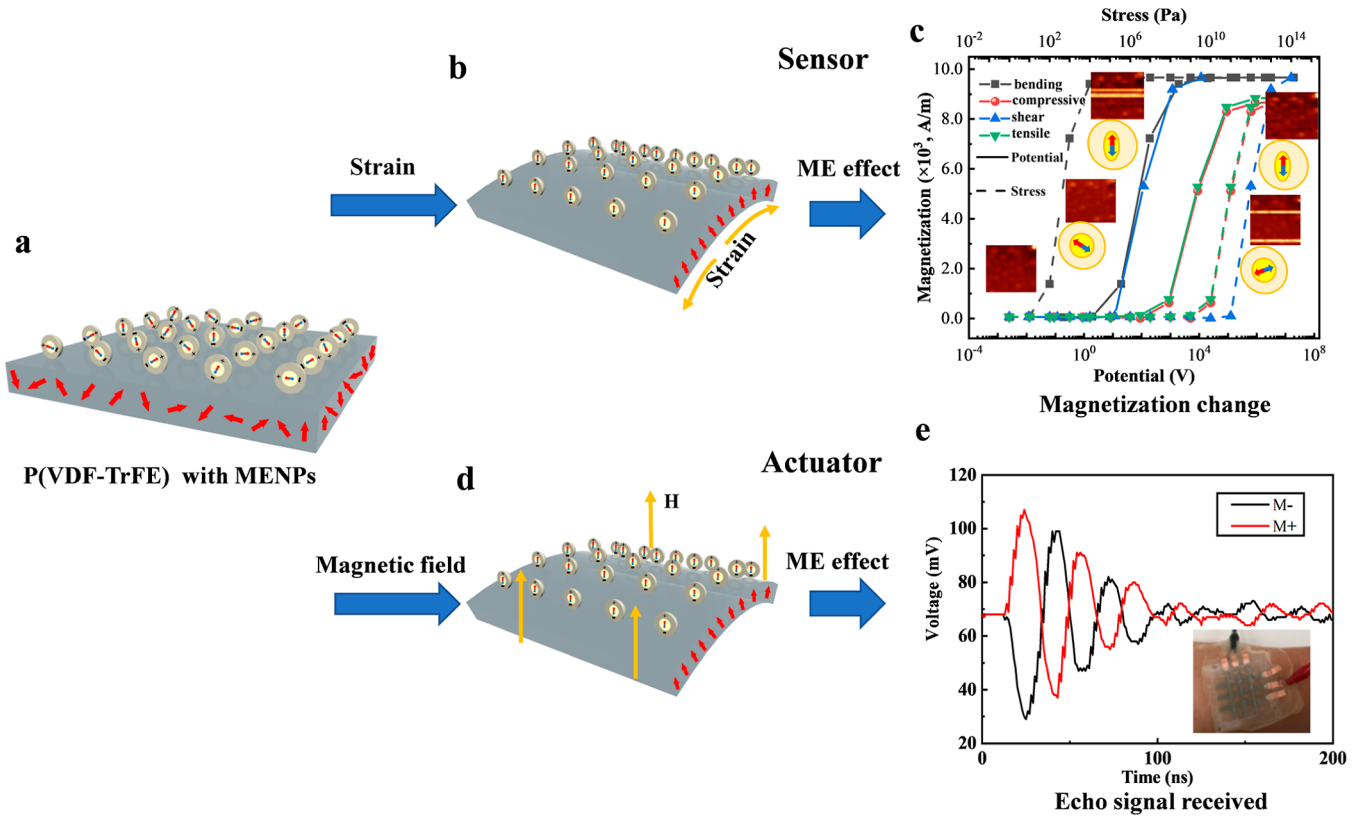

Figure 2. Physical characteristics of the MENP device. (a) Schematic illustration of the MENP patch without mechanical load. (b) Computational simulation results for the stress-generated electric potentials of the bending modes. (c) Resulting magnetization vs potential of MENPs on the patch from bending, compressive, shear, and tensile deformation modes. Changes in the magnetization state of CFO with the potential and stress were applied to P(VDF-TrFE) under different stress cases. (d) Schematic illustration of the MENP patch by applying a magnetic field on the P(VDF-TrFE) with MENPs. (e) MENP patch performance in terms of the electric field generated by applying magnetization.

In order to activate the piezoelectric copolymer film P(VDF-TrFE), a direct current (DC) poling process is implemented by applying a DC voltage to align the surface-bound charge. The entire procedure is depicted in Figure 1b. Initially, the randomly dispersed dipoles can be aligned along the electric field direction. The alignment of dipoles under high electric fields results in surface-bound charges. Compressive and tensile stresses alter the polarization of the film; thus, when mechanical stimuli are applied to the piezoelectric device along the direction of aligned dipoles, electrons at its surface traverse an electrical load. Following poling with a high DC voltage of 2 kV, created devices display clear piezoelectric performance, producing a voltage ranging from 0.1 to 1.5 V as demonstrated in Figure 1c. Throughout this process, we affirm optimal patch performance.

To investigate the potential of multifunctional NPs on wearable surfaces, we initially focused on optimizing the spacing between NPs and determining their ideal response to strain, electric field, or magnetization of MENP patches. Employing an optimal design for MENPs and wearable substrates P(VDF-TrFE), we created MENP patches that contained evenly dispersed $BaTiO_3$@$CoFe_2O_4$ (BTO@CFO) NPs within a P(VDF-TrFE) film. To prepare these patches uniformly, a demagnetization-generating setup was utilized to align the MENPs. We employed P(VDF-TrFE) as a means of controlling the magnetic properties of deposited MENPs; applying a demagnetization field could arrange them accordingly. Figure 1d displays an optimized schematic diagram of the device structure alongside (AFM and TEM) images of said particles. Although FM CFO particles within MENPs are aligned synchronously in terms of magnetic moment orientation, they can still be polarized by external electric fields due to their outer BTO shell; this polarization generates opposite charges at either end of NP shells through ME effect conversion from magnetism into electrical potential and vice versa via BTO layer conversion from electrical fields into magnetism. AFM imaging indicates that precise arrangement is attainable with control over demagnetization fields modulating coffee ring effect tendencies while TEM imaging displays composite structures consisting of roughly 20 nm core−shell composites composed primarily of FE material BTO enveloping FM material CFO inner cores—these types come highly recommended due to their exceptionally high magnetoelectric coupling coefficient when used in patch form.

When a patch is designed, it is crucial to evaluate the strain-mediated magnetization process. Specifically, it is necessary to couple the electric, magnetic, and elastic fields with minimal energy loss. The core−shell-structured NPs exhibit ME effects through applied strain via both magnetorestrictive and piezoelectric effects. By optimizing the NPs, P(VDF-TrFE) substrate, and the distance between them (see details in Supporting Information Figures S4 and S5), we present the final MENP patch functions in Figure 2. In Figure 2a, where red/blue arrows depict changes in magnetization direction (up/down) while P(VDF-TrFE) arrows indicate polarization, randomly oriented magnets are shown at the bottom,

https://doi.org/10.1021/acsnano.4c01102
ACS Nano 2024, 18, 16648−16657

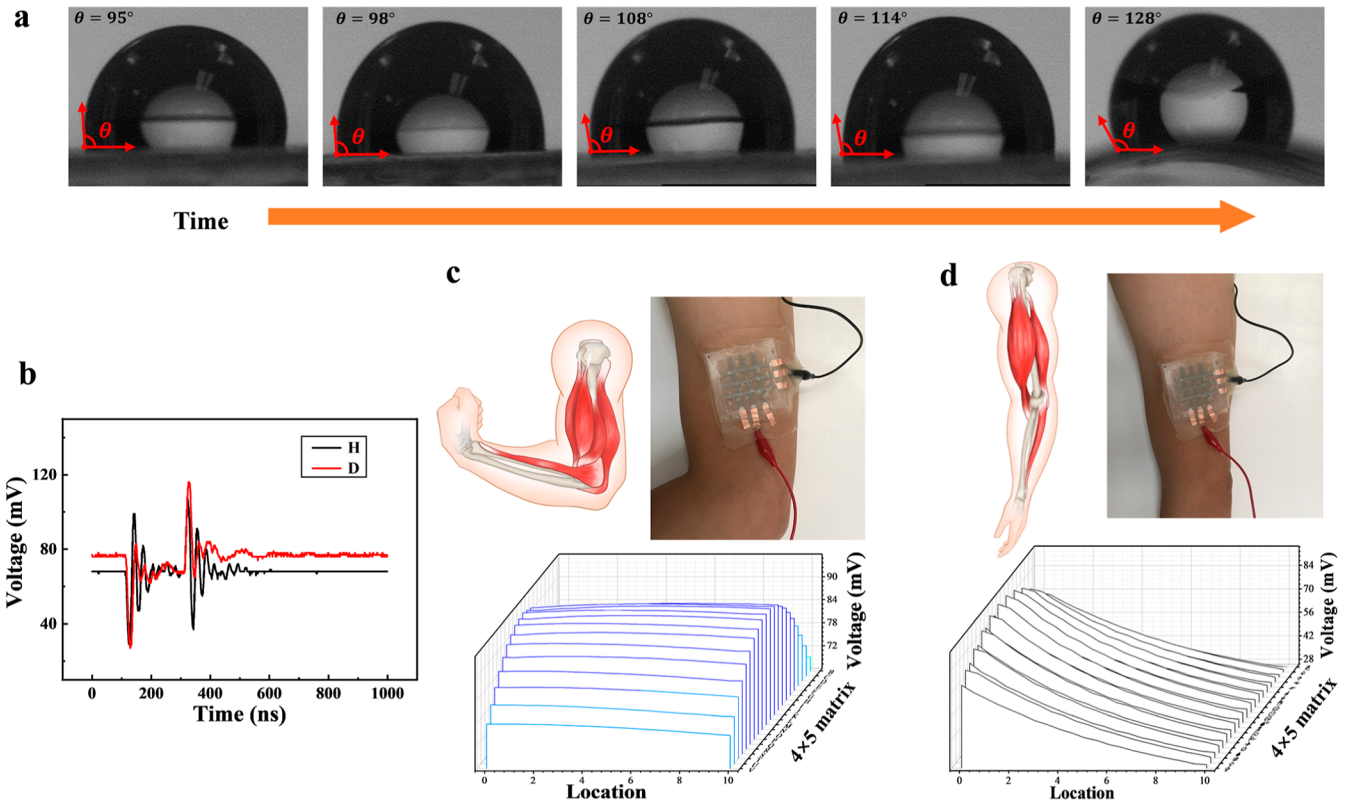

Figure 3. Critical wearable characteristics of the MENP patch. (a) Hydrophobicity of the patch. The water droplet was applied by the time. The angle shows the superhydrophobicity of the patch. (b) Pulse response of the patch. The magnetic signal is measured by applying the pulse. (c) Magnetic field responses induced by flexion modes of the human arm and upon bending, the elbow moves the lower arm toward the shoulder joint until the hand is in level with the shoulder (bicep curl). (d) The magnetic field responses are induced by extension modes of the human arm, and upon extension, the elbow is straightened to lower the hand.

indicating no response from this piezo ME switch in the absence of mechanical load.

By applying strain (indicated by the yellow arrows at the bottom of Figure 2b) to P(VDF-TrFE), an electric potential is generated outside of it. Subsequently, the activated electric field triggers a response in the BTO shell of MENPs, which undergoes strain due to electrostriction. The resulting deformation is then transmitted to the internal CFO, where magnetization orientations tend toward consistency via magnetostriction. So, alterations in the strain could potentially result in the verification of magnetization states, as illustrated in Supporting Information Figure S6. The magnetization under four different modes of deformation—bending, compression, tension, and shear stress—has been analyzed with regard to their influence on generating an electric field for magnetization through P(VDF-TrFE), as shown in Figure 2c. The simulation also shows that the stress generated by bending makes the electric field generated by PVDF larger than that in the other cases, and a smaller stress can be used to change the magnetization state, as shown in Supporting Information Figures S7 and S8. Thus, application of a bending stress is the more efficient approach to switch the magnet. We explore the magnetic−electric (M−E) relationship between P(VDF-TrFE) and CFO NPs; a high density and uniform distribution of NPs are required for inducing magnetization that lays down a technical foundation for reliable wearable MENP patches (see details in Supporting Information Figures S9 and S10).

As shown in Figure 2c, according to the MF curve, the potential generated under the same stress level could overcome the threshold voltage, which could reach saturation magnetization faster. In parallel, various corresponding magnetization states were characterized by low-moment magnetic force microscopy (MFM), as shown in the inset of Figure 2c. And Figure 2c also shows the relationships between the CFO magnetization and the absolute value of the central potential (M-|P|), which indicates the working mechanism from stress, potential, and magnetization. A flexible MENP-deposited patch was used to fabricate a highly sensitive and controllable wearable ME-PZT switch that achieved wearable sensing. As shown in Figure 2d, by applying a magnetic field (yellow arrows) around P(VDF-TrFE), the CFO core becomes strained due to the magnetostrictive effect, and then, the strain is transmitted to the BTO shell and P(VDF-TrFE), which activates electric signals. Figure 2e shows the MENP patch performance in terms of electric field-generated magnetization. Alternating current (AC) magnetic field pulses are generated to enable observation of the resulting electric field. The patch can be used as an actuator driven by a magnetic field.

With the success of the optimized fabrication process, we tested the overall device functions of the MENP patches. For wearable devices, hydrophobicity is important to improve the surface reliability and prevent them from aqueous solutions. Then, the effect could make the device washable to be useful for a practical wearable MENP patch. From Figure 3a, we noticed that the contact angles increased with time (from 95 to 128 degrees of contact angles from left to right, respectively),

https://doi.org/10.1021/acsnano.4c01102
ACS Nano 2024, 18, 16648−16657

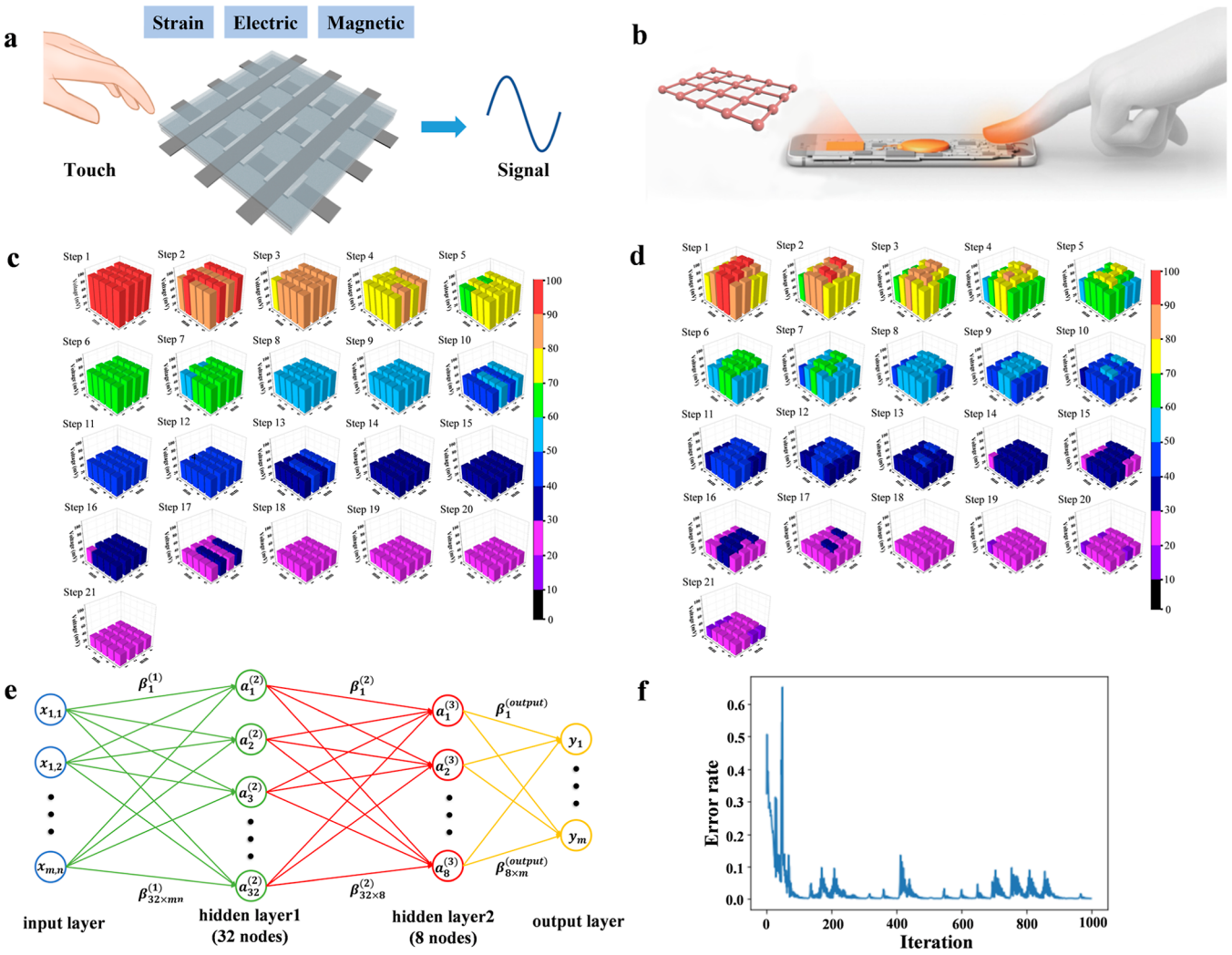

Figure 4. Machine learning-powered performance of the MENP patch for touching. (a) Sensing mechanism of the patch. The signal is generated by the contact. The final signal is received in the form of a magnetic signal. The resulting actuation occurs vice versa. (b) NP function as a node, and the signal is obtained by the average value of the hall sensor. (c,d) The flat and curved surfaces are tested to characterize the shape dependence. (e) Simple neural network (NN) was used to train the system. (f) Loses vs step plot to train the NN algorithm in this case.

and it means that the MENP patch surface becomes superhydrophobic over time (left to right).

Figure 3b shows the MENP patch performance in terms of electric field-generated magnetization. AC magnetic field pulses are generated to enable observation of the resulting electric field. We observe both the first and second magnetic echo signals after the generation of piezoelectricity. This result confirms that the interface between the MENPs and piezoelectric substrate is well linked and operational. As indicated in Figure 2c,d, a generated potential results in magnetization. In this experiment, the opposite conversion from magnetization to an electric field was observed. The received electric signal is due to the elastic deformation of P(VDF-TrFE) caused by the uniform magnetization of the particles.

After checking the superhydrophobicity and electric field-generated by magnetization, the MENP patch sensor is tested as a wearable sensor mounted on the human body, and 3 × 3 matrix sensors are arranged in the MENP region, as shown in Figure 3c,d. Figure 3c,d shows elbow flexion and extension modes, respectively. Body motion-induced magnetic signals are induced via motion from the P(VDF-TrFE) film to MENPs and via electric field generation between the MENPs and the sensors. The resulting magnetic field is observed via a mounted micro-hall sensor array to confirm the magnetization output in real time. Upon bending, the elbow moves the lower arm toward the shoulder joint until the hand is in level with the shoulder (bicep curl), and upon extension, the elbow is straightened to lower the arm. A force of ∼75 N is estimated based on the body motion. As shown in Figure 3c, we observe an electric field range of 120 A/m^2. The experimental tests of the patch match the analyses from the simulation very well. Magnetic field sensors mounted on the instrument are used to detect the field generated by body motion. During the modes, the magnetic field response map is observed using the patch located on the triceps, and the results of contracted (low tension) to relaxed (high tension) are shown in Figure 3c (low tension) and 3d (high tension), respectively. The field response shows that the body motion MENP sensor reliably operates as a motion sensor in a designated way reliably.

The sensing and actuating functions were executed, beginning with the characterization of touch sensor properties.

https://doi.org/10.1021/acsnano.4c01102
ACS Nano 2024, 18, 16648−16657

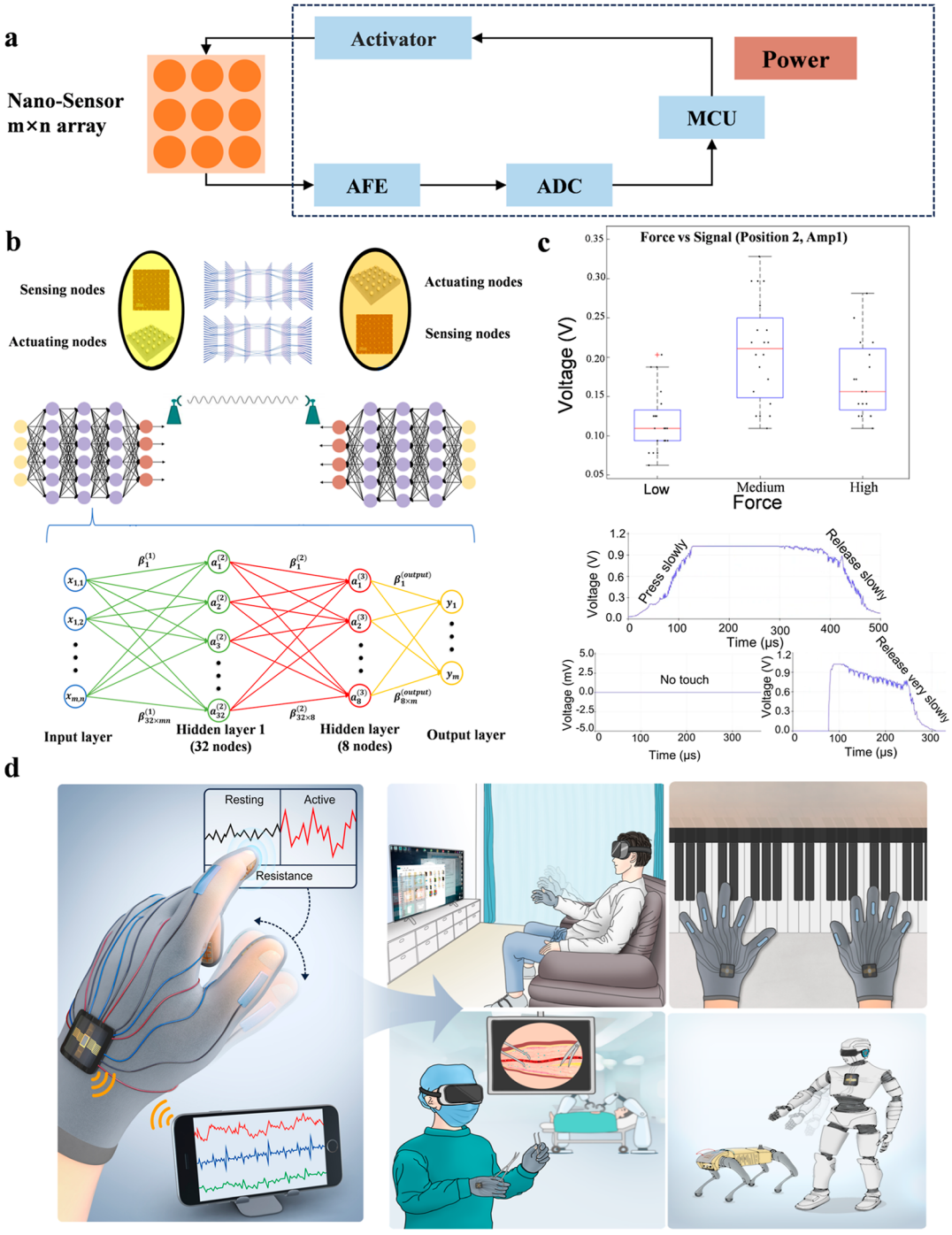

Figure 5. Enhancing the sensitivity of a MENP patch for touching characteristics. (a) Block diagram of the wearable electronic system. The integration and performance assessment of the MENP patch for sensitive touching characteristics is depicted in a comprehensive block diagram showcasing various components. The wearable electronic system includes general-purpose input and output (GPIO), serial peripheral interface (SPI), and system-on-chip (SoC). (b) Through a machine learning algorithm, the sensing signals train the actuation. (c) Diagram of sensing and actuating signals. The resultant data underwent coverts to digital signal through the built-in printed circuit board (PCB) to digital signal format. Subsequently, discrete signals were analyzed to differentiate between varying sensitivities when touched. Here, the touching signal by the force was analyzed and shows that the highly sensitive signals can be obtained by varying the magnitude, duration, and mode of force application. (d) Some possible future applications of the system.

The implementation of *m* by *n* matrix sensor arrays is highly reliant on the intended use cases. This can be demonstrated in Figure 4a,b, which illustrates that incorporating a larger quantity of sensors can yield substantially improved signal sensitivity. Nevertheless, for our particular application, we have selected to utilize a less intricate configuration comprising a 3 × 3 sensor array. By opting for this arrangement, we are assured that we will attain our desired objectives while simultaneously maintaining manageable system complexity. To achieve this, we employed a 3 × 3 matrix sensor array and touched both flat and curved surfaces to assess shape dependence. The outcomes for each surface type are presented

https://doi.org/10.1021/acsnano.4c01102
ACS Nano 2024, 18, 16648−16657

in Figure 4c,d correspondingly. Next, we applied various statistical tools to evaluate our results through simulations. We generated data for every distance between the finger and patch before calculating the average values for each distance while contacting. Figure S11 illustrates an evident monotonic increase trend based on these data points. Although we obtained only the simplest relationship of each distance from the data, we utilized machine learning methods rather than simply fitting a curve with an existing known function; as demonstrated in Figure 4e, a simple NN was used to predict optimal points. Figure S12 and Table S1 illustrate that our model consisted of two hidden layers: one layer had 32 neurons while the other had eight neurons, respectively; both layers were activated using a sigmoid function which can be represented as

$$f(x) = \frac{e^x}{e^x + 1}$$

Moreover, the lost function we used is mean square error (MSE), which is

$$\mathrm{MSE} = \sum_{i=1}^{n} \frac{(\widehat{y_i} - y_i)^2}{n}$$

where y_i is the ground true result distance, while $\widehat{y_i}$ is the predicted result distance that is calculated by the NN. The optimizer utilized here is performed using Adam's optimizer.[41]

After defining the essential parameters, we carried out 1000 iterations and determined from Figure 4f that the loss function had achieved almost perfect convergence. Our evaluation disclosed a loss of approximately 0.0016, and we carefully handpicked three test cases for thorough scrutiny. Table S1 illustrates that the difference between our anticipated values and their actual equivalents is insignificant. Therefore, we have confirmed the NN's proficiency in processing the data sets.

Figure 5a shows that the wearable touch sensing system is fully integrated and was developed through the assembly of the MENP sensor and PCB integration. The system includes a function generator and programmable Bluetooth module that integrates a microcontroller for signal processing and wireless communication. To enable multiplexed sensing, this integrated system incorporates an analog front-end capable of performing multimodal measurements. The transmitted data are analyzed and actuated through the built-in software, as shown in Figure 5b.

Through the integrated system, we first tested the sensitivity of the touching. Figure 5c encompasses all of the data obtained from force plots, specifically focusing on the magnitude of the touching force and the touching mode. The upper plot displays the signal voltage as force increases from low to high using 20 measurements per boxplot. Overall, medium force results in higher voltage readings compared to low force. Additionally, there is sufficient separation between the results indicating differences—higher voltage readings correspond with higher forces applied. However, when high force is used, the voltage lies somewhere between those recorded during low-force application and medium-force application suggesting that there may be a limiting threshold for the touch sensor's responsiveness within which there exists a proportional relationship between voltage reading and applied force. The position at which the pressure is applied also affects the voltage signal, as depicted in Supporting Information Figure S13. Position 3 (well-organized MENPs) shows greater sensitivity compared to positions 1 and 2, which are likely to exhibit similar sensitivity and a comparable number of discrete data points. Furthermore, this sensing system demonstrates high sensitivity in its touching mode, as evidenced by Figures 5c and S14. When the touch is applied slowly, the voltage signal is generated regularly, while a quick touch results in a rapid voltage signal. Additionally, a random touch application leads to a random voltage signal. Moreover, the voltage signal decreases gradually as the touch is released more slowly. It also demonstrates exceptional retention characteristics compared to other piezoelectric sensing systems,[46−48] as its signal can still be maintained for a period even after the touching has stopped.

As depicted in Figure 5d, the potential applications are manifold. In XR applications, the MENP sensors will serve as an input device, akin to the keyboard and mouse that comprise the conventional computer system's input components. Therefore, in such applications, this MENP sensor will function as a crucial piece of equipment for user interaction and control. Additionally, interactive messenger systems can be employed for virtual communication. Numerous other virtual applications are illustrated in the accompanying Figure 5d. The XR glasses can also be used in the field of education, allowing students to experience immersive virtual lessons (piano lessons or training robots by touching sensors and electronic skin type) and simulations. Medical professionals can also benefit from the technology by using it for surgical training and remote consultations. The possibilities are endless, and we can expect to see more market immersible uses for XR glasses in the future.

CONCLUSIONS

We have demonstrated a pliable patch composed of MENPs that serves as a wearable magnetic field system capable of both actuating and sensing electric and magnetic fields induced by strain. The MENP patch's desirable attributes facilitate the development of an ultrasensitive, highly manageable, and wearable MENP device suited for immediate practical applications in daily-use sensors or actuators beyond laboratory settings. This fabricated device affords swift initial training and on-the-fly adaptation, all critical factors for wearable human−machine interfaces where physiological signals vary from user to user. Furthermore, the prepared films exhibit excellent flexibility, microstructural integrity, and strength with ultrahydrophobic surfaces while maintaining their multiferroicity even when subjected to large deformations with extreme curvatures or placed on highly curved moist surfaces, thus indicating the possibility of creating wearable devices utilizing MF materials. This technology may enable various applications requiring low latency and adaptive processing of touching signals such as virtual controllers, interactive messengers, and XR controllers. Our findings suggest that this patch holds potential for emerging metaverse applications.

METHODS

Fabrication and Characteristics of MENP and MEPS. To obtain the PDMS flexible substrate, we first mixed Sylgard 184 and CLA into a mixed solution at a ratio of 10 to 1. Then, the sample was annealed at 150 °C on a hot plate for 10 min to obtain a cured PDMS thin film. The 15 wt % Ag NP solution was spray-coated and embedded in a PDMS substrate. Then, the samples were sintered at 60 °C on a hot plate for 30 min. With regard to P(VDF-TrFE), we used the common spin-coating method, which is considered to be

https://doi.org/10.1021/acsnano.4c01102
ACS Nano 2024, 18, 16648−16657

suitable for manufacturing smooth polymeric coatings for microelectronic applications on an industrial scale. In our work, 2.5 wt % P(VDF-TrFE) was dissolved in DMF and acetone (10:1) mixed solvent and coated on a AgNW-embedded PDMS substrate with UVO exposure for 50 min. The P(VDF-TrFE) film obtained by the spin-coating method and its microstructure and PFM images can be found in Figure 5a. The apparent longitudinal d_{33} was −24 pC/N to −30 pC/N. Figure 5b shows a schematic of the whole flexible substrate obtained. $CoFe_2O_4$ NPs were prepared by a hydrothermal method. In this method, 15 mL of an aqueous mixture of 0.058 g of $Co(NO_3)_2{\cdot}6H_2O$, 0.16 g of $Fe(NO_3)_3{\cdot}9H_2O$, and 0.2 g of polyvinylpyrrolidone was dissolved in 5 mL of aqueous 0.9 g of sodium borohydride at 120 °C for 12 h. Next, a precursor solution of $BaTiO_3$ was prepared by mixing 30 mL of aqueous 0.029 g of $BaCO_3$ and 0.1 g of citric acid with 30 mL of ethonalic solution of 0.048 mL titanium isopropoxide and 1 g of citric acid. $CoFe_2O_4$@$BaTiO_3$ core−shell MENPs were prepared by dispersing 0.1 g of $CoFe_2O_4$ NPs in the precursor solution. The mixture was sonicated for 2 h. The well-dispersed mixture was dried at 60 °C while being stirred continuously overnight. Later, the mixture was subjected to calcination at 780 °C for 5 h. By reducing the cooling rate (controlled by furnace CMF 1100) from above 52 to below 14 °C min^{-1}, the average diameter of MENPs could be controlled from below 25 nm to over 100 nm, with an adequate size distribution of <30%. The particle size distribution was measured by a Zetasizer Nano series via the standard dynamic light scattering approach. For the 25 nm process (14 °C min^{-1} cooling rate), the average size distribution ranged from ∼19 to 31 nm.

To provide mechanical tolerance under various deformations, AgNW network-based nanocomposites were used as intrinsically stretchable interconnects. A AgNW solution of 10 mg/mL concentration in ethanol was spray-coated onto a PEN carrier substrate on which a self-assembled monolayer of (1*H*,1*H*,2*H*,2*H*-perfluorooctyl)silane (FOTS) was deposited as an antiadhesion layer to facilitate transfer of the AgNW networks. The AgNW-deposited PEN substrate was placed on top of uncured PDMS with a curing agent ratio of 20:1. After curing at 100 °C for 1 h, the PEN was peeled off from the cured PDMS, and then, the AgNW networks were successfully embedded on the PDMS substrate. To control the magnetic properties of the MF NPs via the generated E-field, P(VDF-TrFE) was employed due to its ability to convert a mechanical stimulus into electricity. A 20 wt % P(VDF-TrFE) solution in methyl ethyl ketone (MEK) was spin-coated at 1000 rpm onto AgNW-embedded PDMS. A highly crystalline P(VDF-TrFE) thin film was realized by sintering at 140 °C for 1 h in a vacuum oven.

Deposit of MEPS on MENPs. A demagnetization setup was used to deposit MEPS on the MENPs. A drop-cast method was used to deposit MEPS. To eliminate any coagulation, the demagnetization field was modulated to achieve optimal deposition.[38]

Simulation. COMSOL multiphysics, a finite element software program, was used to simulate the strain-induced ME effect based on the structure we proposed above, where PVDF is a 10 μm × 10 μm × 1 μm cuboid, the core radius of the composite nanoparticle is 0.1 μm, and the shell radius is 0.2 μm. In our simulation model, by applying stress to PVDF, an electric field was generated outside it. In this electric field, the shell ferroelectric material of the nanocomposite particle was strained due to the electrostriction effect, and the strain was transmitted to the inner core ferromagnetic material to change its magnetization state due to the inverse magnetostriction effect, which is the so-called ME effect.

SEM and TEM. A TEM with an acceleration voltage of 200 kV was used to take the TEM images. A field-emission gun equipped with an imaging filter (Gatan, GIF200) and DigitalMicrograph software was used. The TEM samples were prepared by placing a drop of mini-emulsion onto a carbon-coated copper (Cu) rid under ambient conditions. SEM (JEOL 9000F) was performed at 15 kV and a working distance of 5 mm.

Scanning Probe Microscopy. The SPM study was performed in noncontact mode by using a Bruker-Nano AFM system. The MFM measurement was conducted in dynamic lift mode with a modulated lift distance.

Integrated System and Data Analysis Procedures. All measurements were conducted at a frequency of 10 kHz with position 1 being furthest away from electrode wiring, while position 3 was closest. Positions 1 and 2 exhibit greater consistency than that of position 3. An increase in the applied force leads to an initial increase in voltage until it reaches a threshold, beyond which any further increase in pressure causes a decrease in measured voltage.

Comparing amplitude values ranging from 0.5 to 2 V shows that an amplitude value of 1 V provides optimal performance. Initially utilizing filtering at ten percent efficacy resulted in reduced noise, but seven percent efficacy revealed more useful information during soft-touch applications despite still removing some noise. An alternative method involving coding complications based on change magnitude could serve as a backup if seven percent filtering proves insufficient when applying filters directly onto devices although not tested thoroughly yet due to its complexity toward the implementation phase.

ASSOCIATED CONTENT

Supporting Information

The Supporting Information is available free of charge at https://pubs.acs.org/doi/10.1021/acsnano.4c01102.

Simulated electric field generated by P(VDF-TrFE); poling and electric field of P(VDF-TrFE); XRD measurement results of high-quality flexible β-phase P(VDF-TrFE) film; M-H hysteresis loops of $CoFe_2O_4$ NPs; simulated electric field distribution diagram at 0, 10, 20, and 40 nm distances; changes in the strain-induced magnetization states; simulated M-H curves; simulated magnetization under different stresses and distances; uniform distribution of NPs and the entire procedure; fabrication processes of the soft piezoelectric device; signal from the touch sensor; neural network structures of our model; touch sensor performance with different position and force; and random touch sensor performance (PDF)

AUTHOR INFORMATION

Corresponding Author

Jeongmin Hong − *School of Sciences, Hubei University of Technology, Wuhan 430068, China; CEE & EECS, UC Berkeley, Berkeley, California 94720, United States;* orcid.org/0009-0008-4190-3157; Email: jehong@berkeley.edu

Authors

Xingjuan Song − *School of Sciences, Hubei University of Technology, Wuhan 430068, China*

Bao Yi − *School of Integrated Circuit, Huazhong University of Science and Technology, Wuhan 430074, China*

Qijun Chen − *CEE & EECS, UC Berkeley, Berkeley, California 94720, United States*

Yifei Zhou − *Department of Mechanical Engineering, UC-Riverside, Riverside, California 92507, United States*

Hyeon Cho − *Department of Electrical and Computer Engineering, Seoul National University, Seoul 08826, Korea;* orcid.org/0000-0002-2381-0335

Yongtaek Hong − *Department of Electrical and Computer Engineering, Seoul National University, Seoul 08826, Korea;* orcid.org/0000-0001-9399-5948

Seungjun Chung − *School of Electrical Engineering, Korea University, Seoul 02841, Korea;* orcid.org/0000-0002-4867-4149

https://doi.org/10.1021/acsnano.4c01102
ACS Nano 2024, 18, 16648−16657

Long You − *School of Integrated Circuit, Huazhong University of Science and Technology, Wuhan 430074, China;* orcid.org/0000-0001-5713-194X

Shaofan Li − *CEE & EECS, UC Berkeley, Berkeley, California 94720, United States*

Complete contact information is available at: https://pubs.acs.org/10.1021/acsnano.4c01102

Author Contributions

J.H. conceived the idea and supervised the experiment. X.S., B.Y., H.C., Y.Z., and S.C. performed and analyzed the data. B.Y., S.L., and J.H. performed the simulation. Q.C., S.L., and J.H. performed machine learning algorithm development. X.S., B.Y., and J.H. wrote the manuscript.

Notes

The authors declare the following competing financial interest(s): SL, QC, and JH filed a patent and founded a company based on this technology.

ACKNOWLEDGMENTS

Work at the Molecular Foundry was supported by the Office of Science, Office of Basic Energy Sciences, of the U.S. Department of Energy under contract no. DE-AC02-05CH11231. Device fabrication and characterization were supported by JS Nano-22-1901119, the School Research Startup fund of Hubei University of Technology (grant nos. XJ2021006101 and GCC20220002), and the National Natural Science Foundation of China (grant no. 62204080).

REFERENCES

(1) Spaldin, N. A.; Fiebig, M. The renaissance of magnetoelectric multiferroics. *Science* **2005**, *309*, 391−392.
(2) Eerenstein, W.; Mathur, N. D.; Scott, J. F. Multiferroic and magnetoelectric materials. *Nature* **2006**, *442*, 759−765.
(3) Ramesh, R.; Spaldin, N. A. Multiferroics: progress and prospects in thin films. *Nat. Mater.* **2007**, *6*, 21−29.
(4) Ratcliff, W. D.; Lynn, J. W. Multiferroics. *Neutron Scattering—Magnetic and Quantum Phenomena*; Academic Press, 2015; Vol. *48*, Chapter 5, pp 291, 338.
(5) Pradhan, D. K.; Kumari, S.; Vasudevan, R. K.; Strelcov, E.; Puli, V. S.; Pradhan, D. K.; Kumar, A.; Gregg, J. M.; Pradhan, A. K.; Kalinin, S. V.; Katiyar, R. S. Exploring the Magnetoelectric Coupling at the Composite Interfaces of FE/FM/FE Heterostructures. *Sci. Rep.* **2018**, *8*, 17381.
(6) Park, T. J.; Papaefthymiou, G. C.; Viescas, A. J.; Moodenbaugh, A. R.; Wong, S. S. Size-Dependent Magnetic Properties of Single-Crystalline Multiferroic $BiFeO_3$ Nanoparticles. *Nano Lett.* **2007**, *7*, 766−772.
(7) Carranza-Celis, D.; Cardona-Rodríguez, A.; Narváez, J.; Moscoso-Londono, O.; Muraca, D.; Knobel, M.; Ornelas-Soto, N.; Reiber, A.; Ramírez, J. G. Control of Multiferroic properties in $BiFeO_3$ nanoparticles. *Sci. Rep.* **2019**, *9*, 3182.
(8) Selbach, S. M.; Tybell, T.; Einarsrud, M. A.; Grande, T. Size-Dependent Properties of Multiferroic $BiFeO_3$ Nanoparticles. *Chem. Mater.* **2007**, *19*, 6478−6484.
(9) Nair, M.; Guduru, R.; Liang, P.; Hong, J.; Sagar, V.; Khizroev, S. Externally Controlled On-Demand Release of Anti-HIV Drug using Magneto-Electric Nanoparticles as Carriers. *Nat. Commun.* **2013**, *4*, 1707.
(10) Silvera Batista, C. A.; Larson, R. G.; Kotov, N. A. Nonadditivity of nanoparticle interactions. *Science* **2015**, *350*, 6257.
(11) Cai, W.; Nix, W. D. *Imperfections in Crystalline Solids*; Cambridge University Press, 2016.
(12) Guo, D.; Xie, G.; Luo, J. Mechanical properties of nanoparticles: basics and applications. *J. Phys. D: Appl. Phys.* **2014**, *47*, 013001.
(13) Khan, I.; Saeed, K.; Khan, I. Nanoparticles: Properties, applications and toxicities. *Arabian J. Chem.* **2019**, *12*, 908−931.
(14) Carlton, C. E.; Rabenberg, L.; Ferreira, P. J. On the nucleation of partial dislocations in nanoparticles. *Philos. Mag. Lett.* **2008**, *88*, 715−724.
(15) Sajanlal, P. R.; Sreeprasad, T. S.; Samal, A. K.; Pradeep, T. Anisotropic nanomaterials: structure, growth, assembly, and functions. *Nano Rev.* **2011**, *2*, 5883.
(16) Reiss, G.; Hutten, A. Magnetic Nanoparticles. *Handbook of Nanophysics: Nanoparticles and Quantum Dots*; CRC Press: Boca Raton, 2010.
(17) Šimánek, E. Far-Infrared Absorption in Ultrafine Al Particles. *Phys. Rev. Lett.* **1977**, *38*, 1161−1163.
(18) Whitesides, G. M.; Mathias, J. P.; Seto, C. T. Molecular Self-Assembly and Nanochemistry: A Chemical Strategy for the Synthesis of Nanostructures. *Science* **1991**, *254*, 1312−1319.
(19) Kralj, S.; Makovec, D. Magnetic Assembly of Superparamagnetic Iron Oxide Nanoparticle Clusters into Nanochains and Nanobundles. *ACS Nano* **2015**, *9*, 9700−9707.
(20) Sun, Y.; Xia, Y. Shape-Controlled Synthesis of Gold and Silver Nanoparticles. *Science* **2002**, *298*, 2176−2179.
(21) Dufresne, A. Nanocellulose: a new ageless bionanomaterial. *Mater. Today* **2013**, *16*, 220−227.
(22) Le Corre, D.; Bras, J.; Dufresne, A. Starch Nanoparticles: A Review. *Biomacromolecules* **2010**, *11*, 1139−1153.
(23) Valenti, G.; Rampazzo, E.; Bonacchi, S.; Petrizza, L.; Marcaccio, M.; Montalti, M.; Prodi, L.; Paolucci, F. Variable Doping Induces Mechanism Swapping in Electrogenerated Chemiluminescence of Ru(bpy) 32+ Core Shell Silica Nanoparticles. *J. Am. Chem. Soc.* **2016**, *138*, 15935−15942.
(24) Taylor, R.; Coulombe, S.; Otanicar, T.; Phelan, P.; Gunawan, A.; Lv, W.; Rosengarten, G.; Prasher, R.; Tyagi, H. Small particles, big impacts: A review of the diverse applications of nanofluids. *J. Appl. Phys.* **2013**, *113*, 011301.
(25) Åkerman, M. E.; Chan, W. C. W.; Laakkonen, P.; Bhatia, S. N.; Ruoslahti, E. Nanocrystal targeting in vivo. *Proc. Natl. Acad. Sci. U.S.A.* **2002**, *99* (20), 12617−12621.
(26) Sung, K.; Mosley, D. W.; Peelle, B. R.; Zhang, S. J.; Jacobson, M. Synthesis of Monofunctionalized Gold Nanoparticles by Fmoc Solid-Phase Reactions. *J. Am. Chem. Soc.* **2004**, *126*, 5064−5065.
(27) Omidvar, A.; RashidianVaziri, M.; Jaleh, B. Enhancing the nonlinear optical properties of graphene oxide by repairing with palladium nanoparticles. *Physica. E* **2018**, *103*, 239−245.
(28) Cheraghian, G.; Wistuba, M. P. Ultraviolet aging study on bitumen modified by a composite of clay and fumed silica nanoparticles. *Sci. Rep.* **2020**, *10*, 11216.
(29) Ghosh Chaudhuri, R.; Paria, S. Core/Shell Nanoparticles: Classes, Properties, Synthesis Mechanisms, Characterization, and Applications. *Chem. Rev.* **2012**, *112*, 2373−2433.
(30) Bai, J.; Wang, J. High-magnetic-moment core-shell-type FeCo-Au/Ag nanoparticles. *Appl. Phys. Lett.* **2005**, *87*, 152502.
(31) Llamosa, D.; Ruano, M.; Martínez, L.; Mayoral, A.; Roman, E.; García-Hernández, M.; Huttel, Y. The ultimate step towards a tailored engineering of core@shell and core@shell@shell nanoparticles. *Nanoscale* **2014**, *6*, 13483−13486.
(32) Zhou, X.; Liu, R.; Qin, S.; Yu, R.; Fu, Y. Current status and future directions of nanoparticulate strategy for cancer immunotherapy. *Curr. Drug Metab.* **2016**, *17*, 755−762.
(33) Biffi, S.; Voltan, R.; Rampazzo, E.; Prodi, L.; Zauli, G.; Secchiero, P. Applications of nanoparticles in cancer medicine and beyond: optical and multimodal in vivo imaging, tissue targeting and drug delivery. *Expert Opin. Drug Delivery* **2015**, *12*, 1837−1849.
(34) Mahmoudi, K.; Hadjipanayis, C. The application of magnetic nanoparticles for the treatment of brain tumors. *Front. Chem.* **2014**, *2*, 109.

(35) Jayathilaka, W. A. D. M.; Qi, K.; Qin, Y.; Chinnappan, A.; Serrano-García, W.; Baskar, C.; Wang, H.; He, J.; Cui, S.; Thomas, S.; Ramakrishna, S. Significance of Nanomaterials in Wearables: A Review on Wearable Actuators and Sensors. *Adv. Mater.* **2019**, *31*, 1805921.
(36) Chung, M.; Fortunato, G.; Radacsi, N. Wearable flexible sweat sensors for healthcare monitoring: a review. *J. R. Soc., Interface* **2019**, *16*, 20190217.
(37) Park, S.; Kim, Y.; Jung, H.; Park, J.; Lee, N.; Seo, Y. Energy harvesting efficiency of piezoelectric polymer film with graphene and metal electrodes. *Sci. Rep.* **2017**, *7*, 17290.
(38) Tu, J.; Min, J.; Song, Y.; Xu, C.; Li, J.; Moore, J.; Hanson, J.; Hu, E.; Parimon, T.; Wang, T. Y.; et al. A wireless patch for the monitoring of C-reactive protein in sweat. *Nat. Biomed. Eng.* **2023**, *7*, 1293−1306.
(39) Hu, H.; Ma, Y.; Gao, X.; Song, D.; Li, M.; Huang, H.; Qian, X.; Wu, R.; Shi, K.; Ding, H.; et al. Stretchable ultrasonic arrays for the three-dimensional mapping of the modulus of deep tissue. *Nat. Biomed. Eng.* **2023**, *7*, 1321−1334.
(40) Hong, J.; Luo, Q.; Jung, D.; Je, S.; Kim, Y.; Im, M.; Hwang, C.; Khizroev, S.; Chung, S.; You, L. Shape transformation and self-alignment of Fe-based nanoparticles. *Nanoscale Adv.* **2019**, *1*, 2523−2528.
(41) Kingma, D. P.; Ba, J. L. Adam: A method for stochastic optimization. *3rd International Conference on Learning Representations, ICLR 2015-Conference Track Proceedings*, 2015; pp 1−15.
(42) Lee, C.; Cho, C.; Oh, J. H. Highly flexible triboelectric nanogenerators with electrospun PVDF-TrFE nanofibers on MWCNTs/PDMS/AgNWs composite electrodes. *Composites, Part B* **2023**, *255*, 110622.
(43) Yang, J.; Chen, Q.; Xu, F.; Jiang, H.; Liu, W.; Zhang, X.; Jiang, Z.; Zhu, G. Epitaxy enhancement of piezoelectric properties in P(VDF-TrFE) copolymer films and applications in sensing and energy harvesting. *Adv. Electron. Mater.* **2020**, *6*, 2000578.
(44) Vacche, S. D.; Oliveira, F.; Leterrier, Y.; Michaud, V.; Damjanovic, D.; Månson, J. A. E. The effect of processing conditions on the morphology, thermomechanical, dielectric, and piezoelectric properties of P(VDF-TrFE)/$BaTiO_3$ composites. *J. Mater. Sci.* **2012**, *47*, 4763−4774.
(45) Joseph, J.; Kumar, M.; Tripathy, S.; Kumar, G. D. V. S.; Singh, S. G.; Vaniari, S. R. K. A highly flexible tactile sensor with self-poled electrospun PVDF nanofiber. *2018 IEEE Sensors*, 2018; pp 1−4..
(46) Lin, W.; Wang, B.; Peng, G.; Shan, Y.; Hu, H.; Yang, Z. Skin-inspired piezoelectric tactile sensor array with crosstalk-free row+column electrodes for spatiotemporally distinguishing diverse stimuli. *Adv. Sci.* **2021**, *8*, 2002817.
(47) Yu, J.; Chen, L.; Hou, X.; Mu, J.; He, J.; Geng, W.; Qiao, X.; Chou, X. Stretchable and skin-conformal piezo-triboelectric pressure sensor for human joint bending motion monitoring. *J. Materiomics* **2022**, *8*, 247−256.
(48) Chung, S. Y.; Lee, H. J.; Lee, T.; Kim, Y. S. A wearable piezoelectric bending motion sensor for simultaneous detection of bending curvature and speed. *RSC Adv.* **2017**, *7*, 2520−2526.

https://doi.org/10.1021/acsnano.4c01102
ACS Nano 2024, 18, 16648−16657